fluids

MDPI

Article

Passive Control of the Flow Around a Rectangular Cylinder with a Custom Rough Surface

Mario A. Aguirre-López [1], Filiberto Hueyotl-Zahuantitla [1,2,*], Pedro Martínez-Vázquez [3] and José Ulises Márquez-Urbina [2,4]

[1] Faculty of Sciences in Physics and Mathematics, Autonomous University of Chiapas, Tuxtla Gutiérrez 29050, Mexico; mario.aguirre@unach.mx
[2] National Council of Humanities, Sciences and Technologies, Mexico City 03940, Mexico; ulises@cimat.mx
[3] School of Engineering, University of Birmingham, Birmingham B15 2TT, UK; p.vazquez@bham.ac.uk
[4] Center for Research in Mathematics, Campus Monterrey, Monterrey 66629, Mexico
* Correspondence: fhueyotl@conahcyt.mx

Abstract: Motivated by existing techniques for implementing roughness on cylinders to control flow disturbances, we performed delayed detached eddy simulations (DDES) at Re = 6×10^6 that generated unsteady turbulent flow around a rectangular cylinder with a controlled wrinkled surface and a 1:4 aspect ratio. A systematic study of the roughness effect was carried out by implementing different configurations of equally spaced grooves and bumps on the top-surface of the cylinder. Our results suggest that groove geometries reduce energy dissipation at higher rates than the smooth reference case, whereas bumped cylinders produce relative pressures characterized by a sawtooth pattern along the middle-upper part of the cylinder. Moreover, cylinders with triangular bumps increase mean drag and lift forces by up to 8% and 0.08 units, respectively, while circular bumps increase vorticity and pressure disturbances on the wrinkled surface. All of these effects impact energy dissipation, vorticity, pressure coefficients, and flow velocity along the wrinkled surface. Both the surface-manufactured cylinders and the proposed visualization techniques could be replicated in a variety of engineering developments involving flow characterization in the presence of roughness.

Keywords: passive control of flow; aerodynamic coefficients; pressure distribution; energy dissipation; wrinkled cylinder; OpenFOAM

check for updates

Citation: Aguirre-López, M.A.; Hueyotl-Zahuantitla, F.; Martínez-Vázquez, P.; Márquez-Urbina, J.U. Passive Control of the Flow Around a Rectangular Cylinder with a Custom Rough Surface. *Fluids* **2024**, *9*, 253. https://doi.org/10.3390/fluids9110253

Academic Editors: Michele Ferlauto and Pier Marzocca

Received: 28 September 2024
Revised: 26 October 2024
Accepted: 27 October 2024
Published: 29 October 2024

Copyright: © 2024 by the authors. Licensee MDPI, Basel, Switzerland. This article is an open access article distributed under the terms and conditions of the Creative Commons Attribution (CC BY) license (https://creativecommons.org/licenses/by/4.0/).

1. Introduction

Passive control measures are often employed to improve the aerodynamics around bluff bodies. Some case studies have required complex modeling approaches for the analysis and interpretation of results, but the majority require simple prototypes such as square and rectangular cylinders. This is the case in energy conversion in marine flow environments, the drag reduction of land vehicles, and the characterization of wind flow around buildings.

For ocean energy conversion, the aim is usually to enhance the amplitude of wave oscillation while maximizing the hydro-kinetic energy by varying the location of one or more cylinder structure [1,2]. This technique is called the VIVACE (Vortex Induced Vibration for Aquatic Clean Energy) converter, and was first reported in references [3–6]. Recent investigations still explore alternatives to optimize the VIVACE device, such as the implementation of secondary structures and channels to redirect the flow [2,7].

In contrast, the design of vehicles with silhouettes that mitigate drag forces commonly targets the delay of the boundary layer separation [8] and aerodynamic optimization through geometrical changes at the front [9,10] and rear of the vehicle [11–13]. An example of successful modifications is presented in Ref. [9], who tested a semi-trailer truck model in a wind tunnel set to a Reynolds number (Re) of $\approx 8 \times 10^5$ to quantify the efficiency of different wind deflectors and side fairings. This experiment enabled drag reductions of 19–29%,

which could translate into 6–8% fuel savings [14]. Other modifications involved the addition of an ancillary to magnify drag, e.g., through external rear view mirrors which enabled increasing force by 3.23% in a modified truck-trailer, as discussed by Chilbule et al. [13]. These examples illustrate areas of opportunity around passive control mechanisms.

Non-applied studies dealing with geometrical changes explore meaningful geometrical changes in test models. For example, Jin et al. [15] proposed cutting the front corners off a squared cylinder to achieve a drag reduction of up to 48–61%; Mazellier [16] added adaptive porous flaps on the upper and lower sides of a square column to reduce energy absorption imparted by the fluid by up to 17–25%; and Malekzadeh et al. [17] placed barriers before a squared cylinder to reduce the mean drag coefficient and the standard deviation of drag and lift by up to 61%, 87%, and 94%, respectively. The first two studies cited here were performed at $\mathrm{Re} \sim 10^4$, whereas the latter was performed at $\mathrm{Re} = 5 \times 10^2$. Some of them proved to have potential applications in ocean engineering.

The manufacture of rough surface patterns for passive control has been explored in a variety of bluff bodies [18,19], more specifically on flat surfaces, as in references [20,21], and airfoils [22,23]. These methods have generated encouraging results: Mariotti et al. [18] achieved a significant delay in boundary layer separation and a reduction in pressure drag when implementing a single groove on the lateral surface of a boat-tailed axisymmetric body; the size of the grooves ranged between 1.5% and 3.3% times the characteristic length of the object. In turn, Qi et al. [19] reported disturbances in the wake of a circular cylinder leading to a reduction in drag and lift of up to 34% and 16%, respectively, when implementing triangular grooves with depths of 2–5% the size of the main body. Moreover, Aguirre-López et al. [24] scrutinized the use of triangular and squared patterns that mimic balconies as passive control measures of flow around tall buildings. These CFD simulations revealed that the facade with balconies displays zig-zag patterns in the pressure and vorticity fields along it, while improving the air circulation at the pedestrian level when the induced roughness covers the lateral walls of the building.

The present work builds on previous research focused on flow disturbances around squared and rectangular cylinders with surface modifications [24,25]. The object of study is a rectangular cylinder with a height-to-length ratio of 1:4 and a height-to-width ratio of 1:1. $\mathrm{Re} = 6 \times 10^6$ was set with the dual purpose of testing new size ratios for ocean engineering purposes while scrutinizing the aerodynamics of commercial buses [26] and other objects with an equivalent geometry and Re. To this end, we completed a systematic study considering bump and groove types to passively modify the aerodynamics of the object. A descriptive analysis of these configurations was carried out, involving pressure, velocity, and energy dissipation variables, while reviewing point, 1D, and 3D flow disturbances. Our numerical simulations were performed in OpenFOAM version 2012 [27], a well-known free open source CFD software that allows for simulating fluid–structure interactions.

The contents of this manuscript are presented as follows. Details of the implementation of geometries, meshing, and the numerical scheme are described in Section 2. The general results of this study are shown in Section 3, while they are discussed in Section 4. The concluding remarks are provided in Section 5.

2. Methodology

2.1. Geometries

The geometry of test cylinders was designed in the open source parametric 3D modeler FreeCAD [28] and subsequently imported into OpenFOAM [27] by means of a formatted stereolithography (STL) file compacted with its `surfaceFeatureExtractDict` tool. The systematic study consisted of 1 smooth rectangular cylinder and 8 modified prototypes.

All cylinders had the same dimensions, namely length $L = 12$ m, height $H = 3$ m, and width $D = 3$ m, with an aspect ratio of 1:4 from a cross-sectional horizontal perspective and 1:1 for the front elevation (aligned with the main flow direction). The characteristic length of the test prototypes was therefore H.

Figure 1 shows the surface roughness implemented in the modified cylinders. The selected wrinkled geometries consisted of ten equispaced prisms of equal shape distributed across the topside of the cylinder. These protruded from the surface to create bumps while penetrating into it to create grooves. Each prism was contained within an imaginary circle with a radius equal to 5% of H, which replicated in the spanwise direction. The shape of each groove symmetrically or anti-symmetrically mirrored its corresponding numbered bump. Similar geometries for both bumps and grooves were designed with a size of 1%, not shown in the figure. The size of all these prisms was selected following Ref. [18] (1.5–3.3%) and Ref. [19] (2–5%), with the purpose of inducing significant flow disturbances.

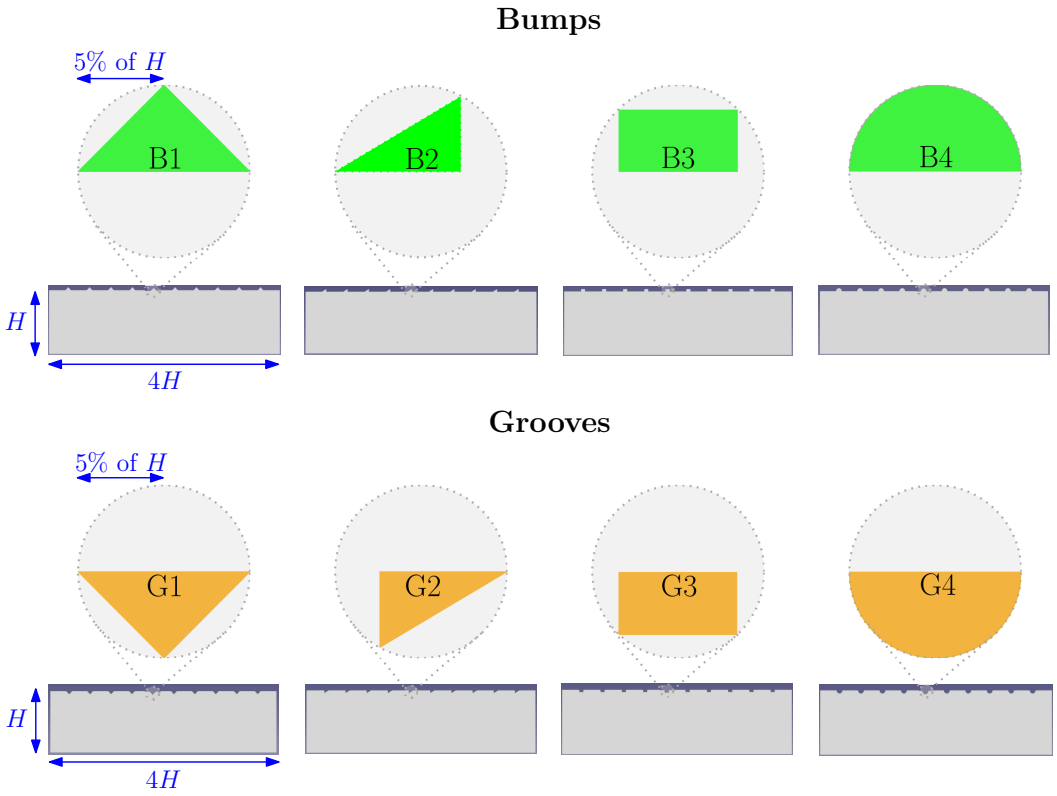


Figure 1. Types of roughness and visualization of their implementation. Bumps are referred to as B1–B4, while grooves are referred to as G1–G4. Each of them spans the cylinder in the spanwise direction.

2.2. Computational Array and Problem Description

The computational domain is shown in Figure 2. The origin of the global Cartesian system is located at the center of the cylinder and the flow runs parallel to the x-axis. Inflow and outflow boundaries were defined at $x = -6H$ and $x = 11H$, respectively. In turn, symmetry boundaries were implemented in the front and back and up and down limits, located at $y = \pm 4.5H$, and $z = \pm 4.5H$, respectively. The walls of the cylinders abided by the non-slip boundary condition.

The simulations started with a free stream velocity equal to $U_\infty = 10$ m/s in x-direction and a kinematic pressure $p = 0$ m^2/s^2 in the internal field, while a kinematic viscosity $\nu = 5 \times 10^{-6}$ m^2/s was considered. These settings corresponded to Re = $U_\infty H/\nu = 6 \times 10^6$. Maintaining H and changing to standard atmospheric conditions (at 20 °C), the above Re led to an equivalent characteristic velocity of $U^*_\infty \approx 30$ m/s, leading to a Mach number (M) of M $= U^*_\infty / c_s = 0.09$, with c_s as the speed of sound, which justifies the incompressibility of the simulated flow [29].

The boundary conditions presented in Figure 2 were computed by fixing U_∞ and a zero-gradient condition for p at the inlet. In turn, a fixed value of $p = 0$ m^2/s^2 and a composed condition for **U** were set at the outlet; the latter consisted of switching between

a zero gradient when the fluid escaped the domain and a fixed value of $|\mathbf{U}| = 0$ when the fluid flowed into the domain. This was achieved by using the option `inletOutlet` from OpenFOAM. Finally, no-slip and zero-gradient conditions were set for **U** and p at the cylinder's boundary.

The mesh contained a mix of structured and non-structured grids, which can be seen in Figure 3. The coarsest grid denoted a uniform-structured section tagged by Zone A, conformed with quasi-cube cells with an approximate volume of 1 m^3, i.e., $H/3$ per side. Zone A was constructed with the `blockMesh` tool in OpenFOAM, while the rest of the grids were constructed by means of the `SnappyHexMesh` tool. Zone B also consisted of a uniform-structured grid but with higher refinement for capturing flow effects in the wake more accurately. The grids enclosing Zones C, D, and E were designed to further refine measurements when approaching the cylinder, with all of these planned to be non-structured. Zone E encloses the finest grid consisting of the cells intersected by the cylinder edges, allowing us to capture the geometry of the grooves and the bumps with an approximate resolution of $H/384$; in turn, Zone D was formed of cells that defined the imported STL-geometry, while Zone C was a scaled volume that diminished resolution while spanning from the ending of Zone D to a radial distance $2H$ from the cylinder's walls; it also matched the refinement of Zone B at $0.5H$ from the walls. The referred software built the mesh in a way that, when two different refinement levels were superposed, the higher one was implemented. A space of one cell (of the lower level) was left at the transition between refinement levels.

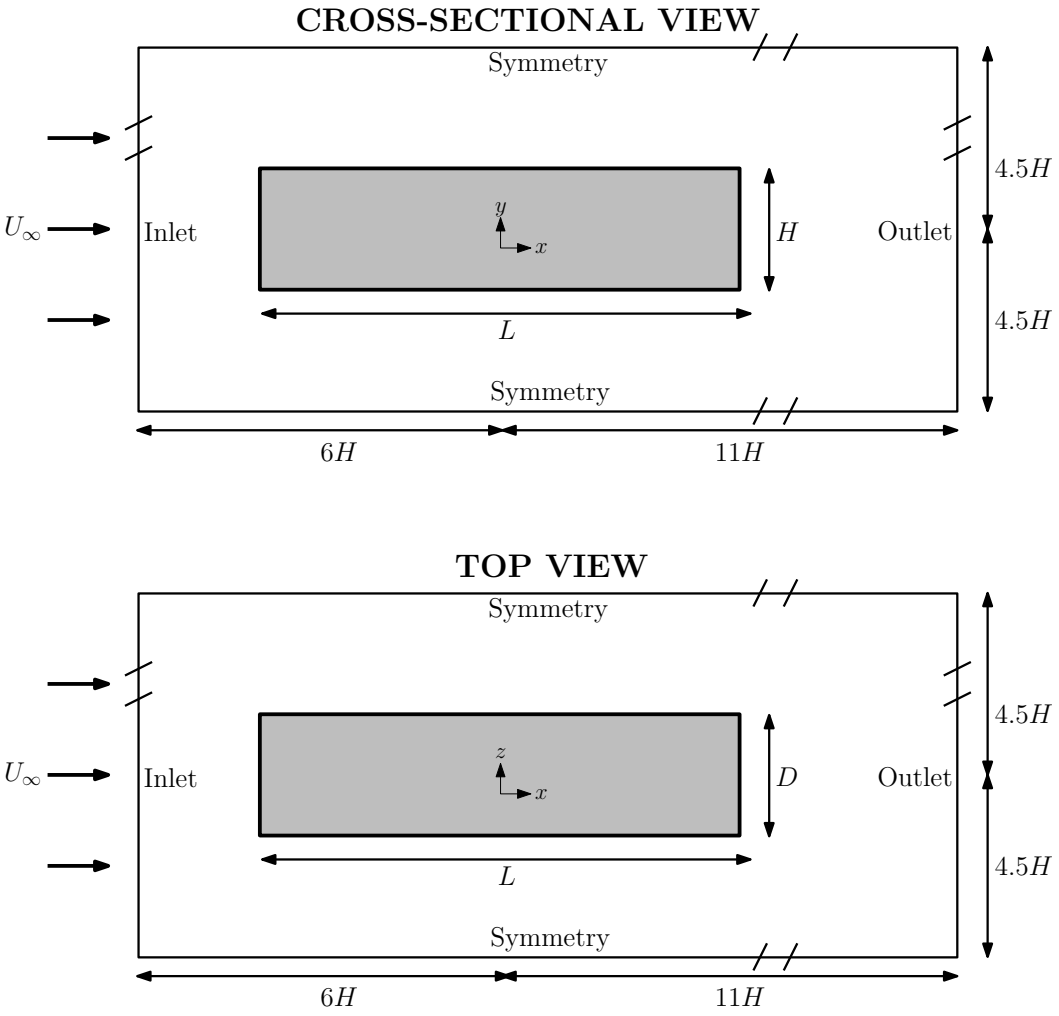


Figure 2. Illustration of the computational domain.

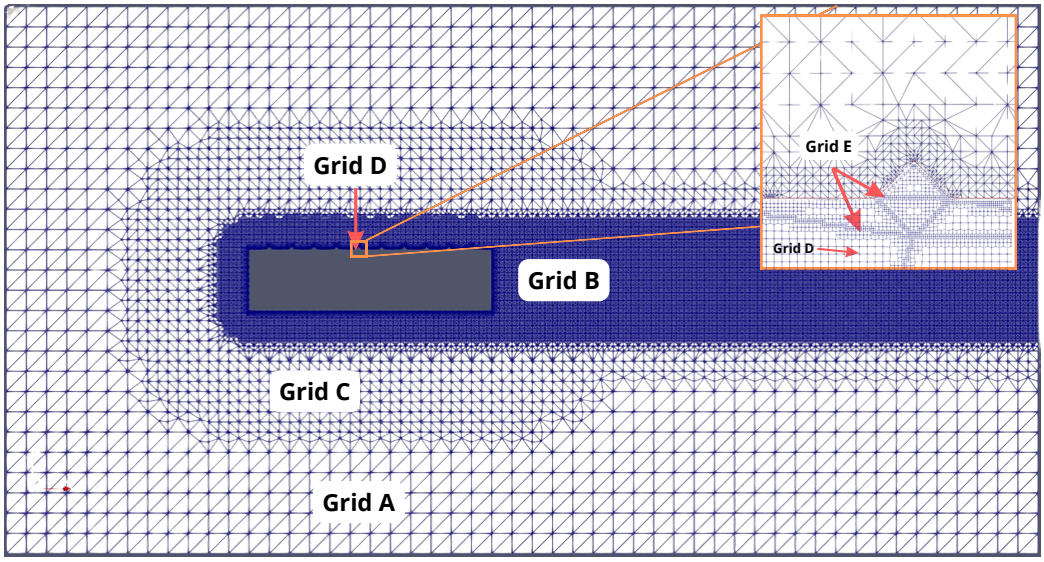


Figure 3. Grids of the computational array. The inset shows a zoom in around a triangular protuberance to see Zones D and E.

2.3. Numerical Scheme

To carry out delayed detached eddy simulations (DDES), we used the Pressure Implicit with Splitting of Operators (PISO) solver in OpenFOAM, named `pisoFOAM`. This solver allowed us to reproduce the unsteady-incompressible-isothermal flow, taking advantage of the computational speed of Reynolds-average simulations (RAS), and switched to large scales when approaching the cylinder with large eddy simulations (LES), considering a smooth transition between both scales with the delayed-detached feature. Moreover, we merged the DDES scheme with the Spalart–Allmaras (SA) model, which was originally designed for simulating flows around airfoils, based on a equation of turbulent viscosity (ν_t) [30,31]. The general coupling of the numerical scheme is given by the SA equation:

$$\frac{D}{Dt}(\rho\tilde{\nu}) = \nabla\cdot(\rho D_{\tilde{\nu}}\tilde{\nu}) + \frac{g_{b2}}{\sigma_{\nu_t}}\rho|\nabla\tilde{\nu}|^2 + g_{b1}\rho\tilde{\zeta}\tilde{\nu} - g_{w1}f_w\rho\left(\frac{\tilde{\nu}}{\tilde{d}}\right)^2 + \zeta_{\tilde{\nu}}, \tag{1}$$

where ν_t is pulled from a nonlinear function of the modified turbulent viscosity ($\tilde{\nu}$), so that $\nu_t = \tilde{\nu}f_{\tilde{\nu}1}$, with $f_{\tilde{\nu}1} \equiv f_{\tilde{\nu}1}(\tilde{\nu})$ as a damping function depending on the distance to the nearest wall and other factors; ρ is the density of the fluid; ζ refers to the shear stress; and $\tilde{d}$ defines the length scale. To switch between RAS and LES schemes, we used the following rule:

$$\tilde{d} = \max[L_{RAS} - f_d, \max(L_{RAS} - L_{LES}, 0)], \tag{2}$$

with the RAS scale (L_{RAS}) being a function of the distance from the analyzed cell to the closest solid wall and the LES scale (L_{LES}) being a function of the local grid spacing and a modified low Reynolds number. The smoothness of the transition was controlled by the hyperbolic-tangential function f_d.

In this context, our solution methodology allowed the discretization of the Navier–Stokes equations and the SA equation via the finite volume method (FVM), taking into account a conditionally stable second-order implicit-backward interpolation for time schemes, Gauss linear interpolation for gradient schemes, Gauss linear limited interpolation for divergence and Laplacian schemes, and linear interpolation to transform the cell-center quantities to face centers.This produces a system of algebraic equations of the form $A\mathbf{x} = \mathbf{b}$, where $A \equiv$ coefficient matrix, $\mathbf{x} \equiv$ vector of variables, and $\mathbf{b} \equiv$ source vector, which is solved by `pisoFOAM` through an implicit predictor and multiple explicit corrector steps, seeking to obtain close approximations of the exact solution of the difference equations at each time-step [32]. In this part, the algorithm works in a fully implicit pressure scheme with the

coupling of the velocity and pressure equations being handled through the iterations [33,34]. We set a maximum of three corrections without extra-correction for mesh non-orthogonality, while the resulting algebraic equations were solved via different methods: a generalized geometric-algebraic multi-grid (GAMG) solver method for pressure, with a Gauss–Seidel method as a smoother; a preconditioned pipelined conjugate residuals (PPCR) solver to override solution tolerance for the final pressure; and a symmetric Gauss–Seidel solver for the rest of the variables.

Regarding the values of parameters, the turbulent viscosity was initialized with $\nu_t = 0$ in the entire domain and calculated (boundary condition) using the function `nutUSpaldingWallFunction` at the cylinder's walls. In turn, the modified turbulent viscosity was set to $\tilde{\nu} = 5\nu$ in the entire domain, except for cells near to the cylinder's wall, in which $\tilde{\nu} = 0$ m^2/s, as usually followed by the Spalart–Allmaras model [35,36]. For consistency with the high Re we were dealing with, a uniform turbulence intensity of $I = 15\%$ was also defined at the inlet [37], which led to a turbulent energy of $k = (3/2)(U_\infty I)^2 = 3.375$ m^2/s^2.

A full definition of all variables in Equation (1) and other implicit parameters in the model is given in references [35,38], including the parameters cited above, the solver mechanisms, the meshing techniques, and the map default values of the *motorbike* example in OpenFOAM-v2012 (Directory: `OpenFOAM/OpenFOAM-v2012/tutorials/incompressible/pisoFoam/LES/`). The reader is referred to the OpenFOAM tutorials [39] for more details on similar flow simulations, and to our previous works [24,25], in which our current computational–mathematical array is applied and validated by means of a resolution study dealing with a squared cylinder at Re = 2.14×10^4 and a comparison with experimental results focused on buildings subject to a flow regime between Re = 1.59×10^7 and Re = 4.01×10^7, which covers the Re used in our current case study.

2.4. Validation and Nomenclature

With the aim of standardizing data representation, the units in the graphics and results are dimensionless, e.g., $(X, Y, Z) = (x, y, z)/H$, $U \equiv (U_x, U_y, U_z) = (u_x, u_y, u_z)/U_\infty$, $\Omega = (\omega H)/U_\infty$ (vorticity), $N_t = \nu_t/(U_\infty H)$, and $T = (tU_\infty)/H$. Drag Cd and lift Cl dimensionless coefficients were directly obtained from OpenFOAM by referring to the library *libforces.so* of the function *forceCoeffs* in the directory `controlDict`. The relative-pressure coefficient was computed using the known formula

$$Cp = \frac{p - p_\infty}{0.5\rho U_\infty^2}, \tag{3}$$

where the freestream pressure p_∞ is consistent with the initial pressure condition.

Table 1 shows the number of cells contained within the computational arrays that result from implementing the geometries described in Section 2.1 using the mesh parameters discussed in Section 2.2. According to this, wrinkled cylinders occupy a larger quantity of cells given the refinement needed to shape each bump/groove. In this sense, meshes with circular modifications (B4 and G4) increase cell numbers by up to 41–45% compared to the smooth case. Below these, we see the squared modifications (B3 and G3), with a 27–28% increase, and the two types of triangular modifications (B1, B2, G1 and G2), with a 19–22% increase above the smooth case.

In addition to the validation cases mentioned in Section 2.3, we initialized the present simulations by pre-testing the case B4 with three lower refinements near the object: a coarse mesh (with 55% fewer cells than our smooth case, and a maximum resolution of $H/24$), a medium mesh (with 50% fewer cells and $H/48$ in resolution), and a fine mesh (with 10% fewer cells and $H/96$ in resolution), and a same-level refinement but adding more temporal refinement (from $\Delta T = 1 \times 10^{-3}$ units to $\Delta T = 6.67 \times 10^{-4}$). Coarse, medium, and high meshes apply their corresponding maximum resolution to Grids B, D, and E (see Figure 3); then, the high mesh differs from the extra-high one only in the refinement level for Grid E. Figure 4 shows the convergence of our computational array

when calculating the aerodynamic coefficients; Ext. high2 array refers to the extra-high one with $\Delta T = 6.67 \times 10^{-4}$. Although convergence is achieved with the high mesh, we selected the extra-high (Ext. high) mesh as an extra measure of security to adequately capture the wrinkled geometries of the non-smooth cases. From this point on, we will use the term "benchmark" to refer to the wrinkle-free cylinder modeled by using the extra-high mesh.

Table 1. Number of cells of each test case.

Geometry	# of Cells
Smooth (benchmark)	1,695,959
B1	2,064,356
B2	2,050,865
B3	2,176,280
B4	2,457,100
G1	2,035,171
G2	2,021,147
G3	2,152,050
G4	2,382,913

The validation of the model was performed in terms of the energy contents of the drag and lift pressure fluctuations across a frequency range f for the case B4, using the Ext. high mesh. Figure 5 shows the autoscaled power density function (PSD), in which we can observe a broadband energy that characterizes turbulent flow. These results show how the low-frequency fluctuations associated with larger eddies or gusts are followed by the inertial range (highlighted in black), covering the range $f = 10^{-4}$–10^{-3} Hz. The spectral power distribution satisfies the transference of energy according to Kolmogorov's scaling law. We can also note that the energy dissipation rate takes place at the highest frequencies, obeying a faster decay due to the turbulence of smaller eddies.

Then, by using the OpenFOAM utility `mapFields`, we mapped the high-mesh solution at time $T = 200$ to start the fine tests (those referred to in Table 1). This enabled us to avoid an increase in the transition interval for the stabilization of the flow, which permitted a larger sampling interval. The total time simulation of the fine tests also matched 200 units. Figure 6 allows us to exemplify this by showing the variation in the drag Cd (a) and lift Cl (b) coefficients obtained for the fine-smooth case in superposition to those calculated with the modified geometry. The sampling interval started from $T = 20$ to ensure that the flow was stable for all runs as well as for both the Cd and Cl series, which were obtained by referring to the function `forceCoeffs` of the library `libforces.so`, evaluating Equations (4) and (5):

$$Cd = \frac{Fd}{0.5\rho DHU_\infty^2}, \tag{4}$$

$$Cl = \frac{Fl}{0.5\rho DHU_\infty^2}, \tag{5}$$

where Fd and Fl are the force acting on the building in the streamwise and transverse directions, respectively.

The Courant number was kept below 1 with the corresponding grid and time discretization of the Ext. high mesh. In each time step and each velocity component, the convergence criteria were set at 1×10^{-6} for pressure and 1×10^{-7} for turbulent kinematic viscosity in their respective units. Each simulation ran in parallel across the 24 subdomains, by using the `scotch` method from the `decomposeParDict` tool in OpenFOAM. We used a cluster with Intel® Xeon® CPU E5-2680 v3 at 2.50 GHz with 48 Cores and 131.072 GB RAM. Under these conditions, the computational time was around 2 days for the benchmark and up to 3 days for the wrinkled cases discussed in the following sections.

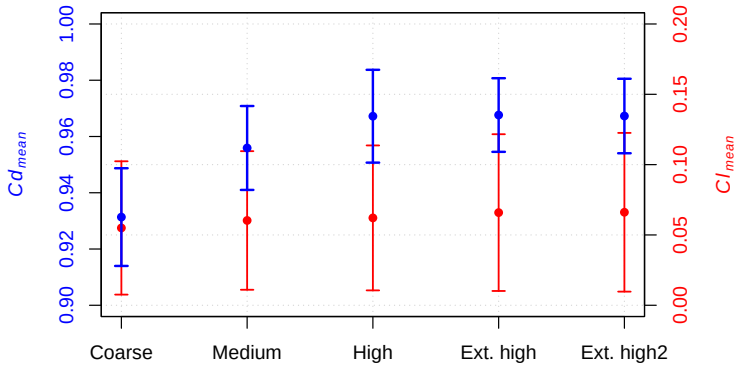


Figure 4. Time-averaged coefficient values for different mesh arrays and their standard deviation with error bars for drag *Cd* (blue) and lift *Cl* (red).

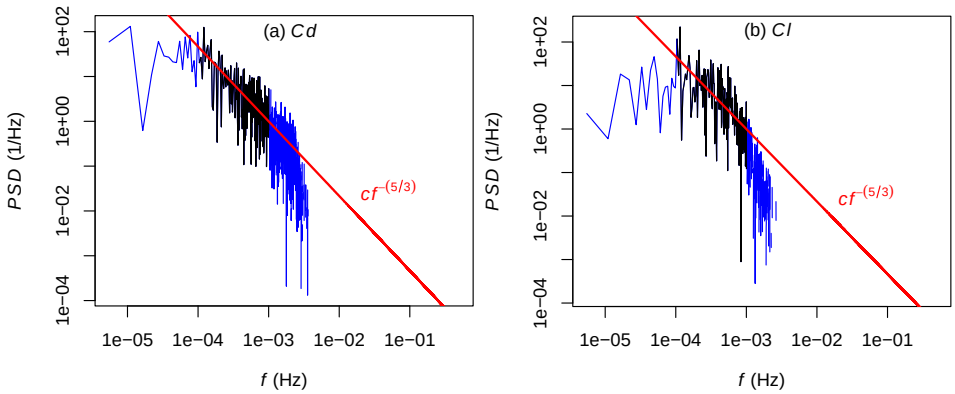


Figure 5. Log–log plot of the auto-scaled power spectral density of (**a**) drag and (**b**) lift series of the case B4 using the Ext. high mesh. The inertial range is approximated in black. Negative *PSD* values are omitted due to the logarithmic transformation. Kolmogorov's scaling law is plotted in red, considering a constant $c = 10^{-5}$ for both series.

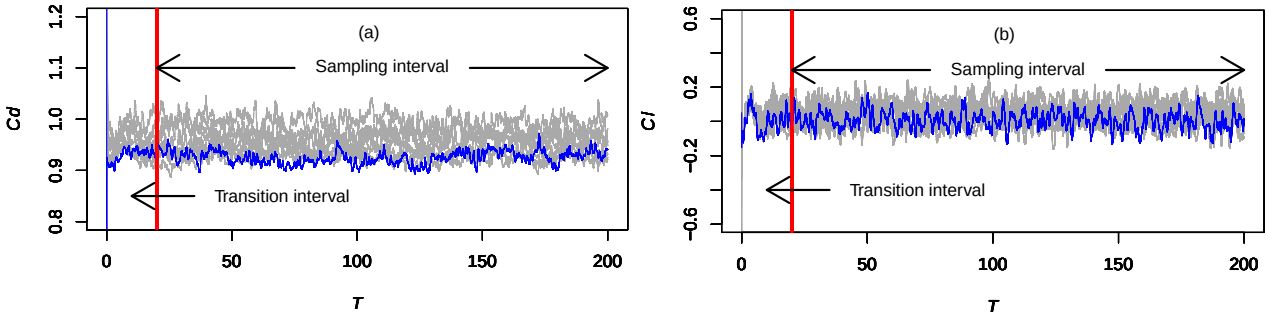


Figure 6. *Cd* (**a**) and *Cl* (**b**) time series indicating the dimensionless time from which the sampling interval starts. The benchmark is plotted in blue.

3. Numerical Results of the Surrounding Flow

Figure 7 shows the average velocity maps U_{mean}, combined with contour maps of pressure coefficients Cp_{mean}. For all geometries, the sharpness of the main body causes the flow to display a separation at the top-left corner of the cylinder ($X = -2$), followed by its corresponding return halfway up the cylinder ($X = 0$). This involves a large zone of vorticity that is reflected by the closed iso-pressure contours that extend up to the position corresponding to the fourth groove/bump ($X \approx -0.5$) and more than one characteristic length D in the upward direction. Outside this zone, the main time-averaged disturbances (large and small) caused by the geometries occur.

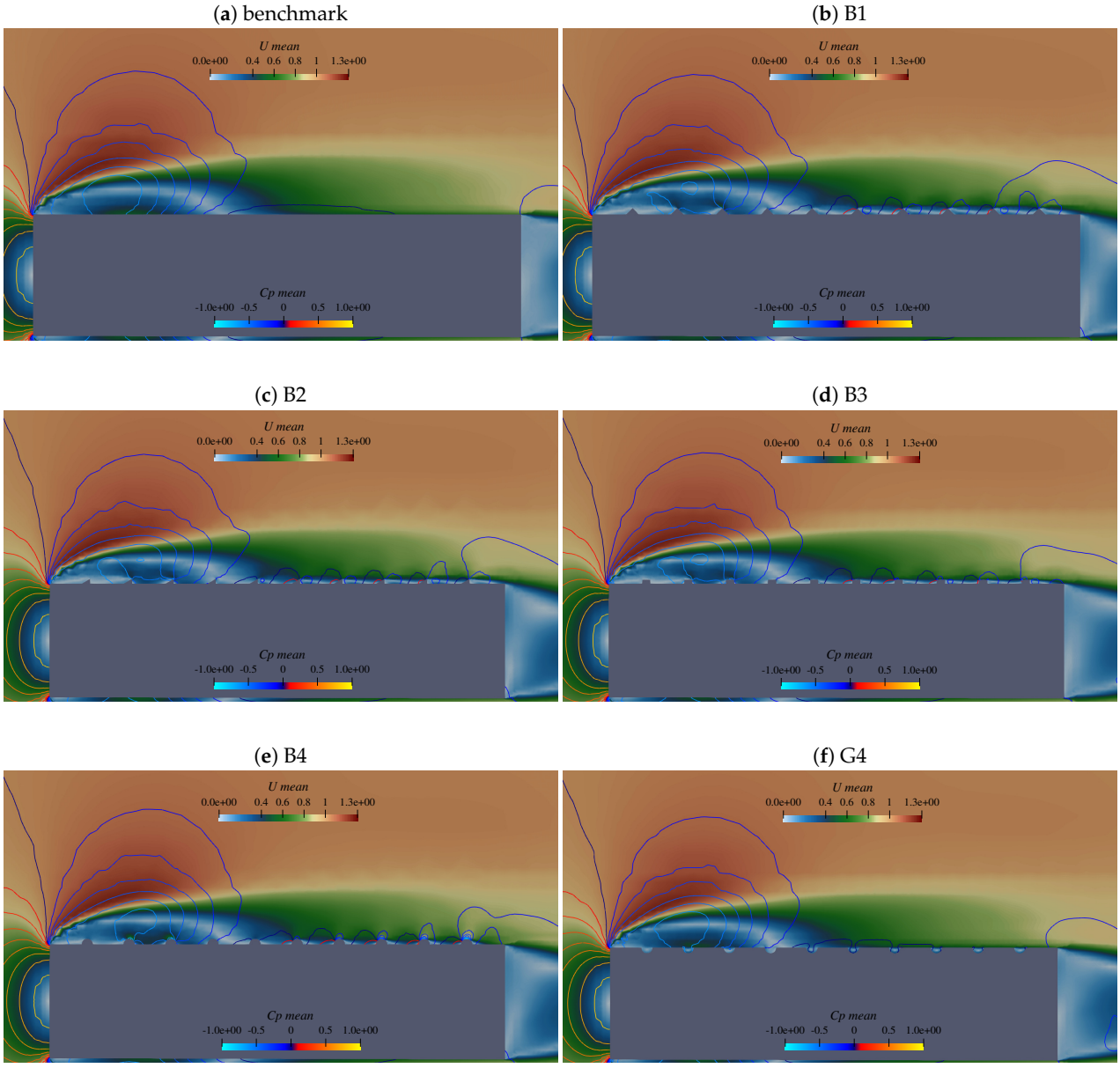


Figure 7. Cross-sectional view of the solutions, showing the color maps of U_{mean} and the contour lines of Cp_{mean} for some considered geometries. Benchmark (**a**). Bumps (**b**–**e**). Circular grooves (**f**). The rest of the groove geometries are not included due to their similarity with the flow patterns of the shown case.

On a large scale, all of the modified geometries disturb the flow symmetries seen in the benchmark around the cylinder. In general, the effects produced by bumps are greater than those produced by grooves. Despite the fact that the bumps caused a break in the iso-pressure contour of -0.8 units (sky blue contours) in the vortex zone mentioned above, the flow at the front and bottom of the cylinder showed no significant disturbances in the immediate and middle zones, so we will focus on the upper part of the cylinder.

On a smaller scale, around the modified surface topology, it is also observed that the presence of bumps caused larger, perhaps more interesting, disturbances to the flow than the induced grooves. The latter fold the near-zero contour lines inside the six rear grooves. In contrast to this, it is worth highlighting an up–down effect on pressure that became particularly visible around the last five bumps. For triangular cases (B1 and B2), high-pressure zones (red contours) are located before every bump, while low-pressure zones (blue contours) clearly developed around their rear, which was assumed to be related

to a softening flow separation. In turn, for the squared and circular cases (B3 and B4), high pressures share the front of each bump with zero-level pressures (dark contours), while very low pressure contours predominate on the exact position and rear side of the bumps. Contrasting with triangular cases, this observed transition of pressure zones suggests a quick flow separation caused by the bluff shape of the bumps.

4. Discussion and Deeper Analysis

4.1. Point Effects: Flow–Structure Interaction

In Figure 8, we plot the time-averaged Cp_{mean} versus standard deviation Cp_{std} coefficient pressure calculated by (3), to highlight the observed small-scale effects. The graphics span half of the cylinder surface, from the front to the rear, as drawn in the picture. For all geometries, the highest pressure $Cp_{mean} = 1$ occurs on the front side, and then reduces to a value $Cp_{mean} = -0.5$ at the top-left corner where the flow separates. Then, pressure reduction continues until $X = -1.3$, where it reaches different local minimums depending on the geometry. From that point, we see a pressure increase until $Cp_{mean} = 0$ at $X = -0.3$ due to the reattachment of the flow. For the benchmark (a), the pressure stabilizes without vorticity until the rear side ($X = 2$), while the associated standard deviation only increases in the transition zone $-1.3 < X < 0.3$.

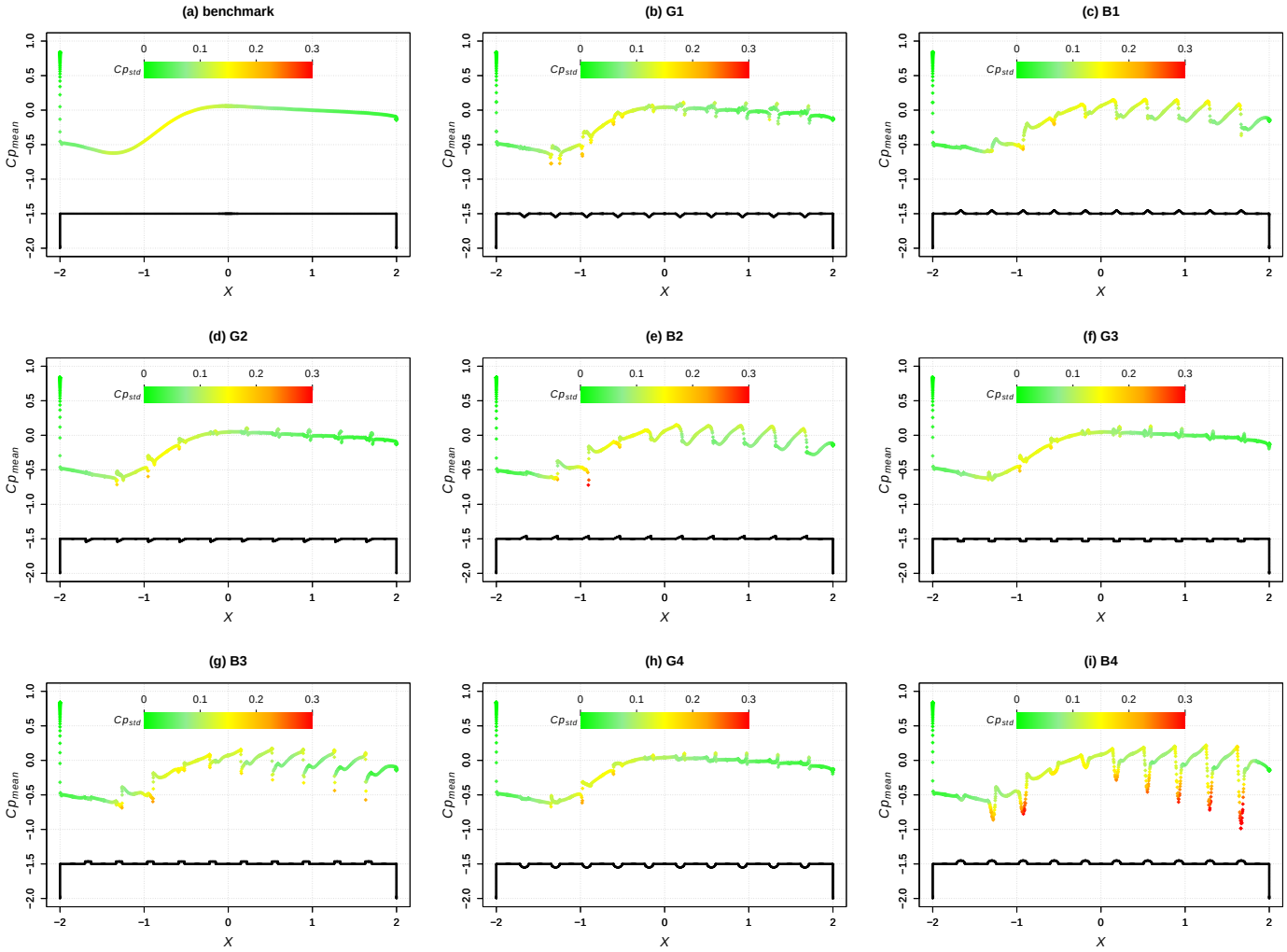


Figure 8. Cp_{mean} values on the top surface of the cylinder at the z-central line along the x-axis. Cp_{std} values are also shown by the color scale. Benchmark (**a**). Grooves (**b**,**d**,**f**,**h**). Bumps (**c**,**e**,**g**,**i**).

As pointed out above, cases G1–G4 only disturb the mean flow at the location of the grooves (small-local changes in Cp_{mean}), but they produce larger variations in Cp_{std}

than the benchmark around the transition zone and beyond. As observed in Figure 7, this performance originates past the first groove where small eddies appear, without altering the overall pressure pattern established by the main flow, which is equivalent to the effect produced in a continuous flow by a small cavity, acting as a controller of flow separation, avoiding a cascade effect. This process is replicated across the grooved region since the main flow dominates, which is the reason why the pressure envelope resembles that of the benchmark.

In turn, the structured contour lines observed with the configurations B1–B4 show a sawtooth pattern of Cp_{mean} from the middle ($X = 0$) to the rear side ($X = 2$) of the cylinder. The smooth transition to local highs of the sawtooth pattern takes place over the zones with a flat surface, whereas the transitions to local lows are steeper over the bumps. In agreement with the observations illustrated in Figure 7, the pattern is smoother and lower in amplitude for the triangular cases (B1 and B2), where the maximum disturbances reached are about 0.2 dimensionless units, which fluctuate symmetrically with respect to the zero line, while their standard deviations oscillate between approximately 0 and 0.15. For cases B3 and B4, the largest local decreases in Cp_{mean} occur with the highest values of Cp_{std}, overall increasing their magnitude with their proximity to the last bump to reach $Cp_{mean} = -0.6$ and $Cp_{std} = 0.25$ for B3, and $Cp_{mean} = -1$ and more than $Cp_{std} = 0.3$ for B4. Furthermore, the sharpness of the rough geometries leads to the highest Cp_{std} values occurring at the Cp_{mean} peaks (before bumps) for B1–B2, whereas they occur at the Cp_{mean} valleys (over bumps) for B3–B4.

This performance suggests an accumulation of uncontrolled flow redirection caused by the bluff bumps. However, the separation between bumps is large enough to maintain flow separations in a local or point scale, the reason being that the general sawtooth structure is always in phase according to the equally spaced roughness at the middle-rear side, hence the quasi-harmonic pressure configuration.

4.2. Three-Dimensional Effects: Aerodynamic Coefficients and Results Compilation

Figure 9 shows a different perspective regarding the small and large disturbances observed in the mean aerodynamic coefficients Cd_{mean} and Cl_{mean}. No geometrical change reduced drag with respect to the benchmark. The grooves caused slight increments of no more than 1%, whereas higher increments ranging from 4% to 8% were reached in the presence of bumps, namely 4% (B3), 5% (B4 and B2), and 8% (B1). Similar effects are seen for the lift coefficient. Cl_{mean} increases by less than 0.02 units for groove cases, while it increases by 0.06 units for B3 and B4, 0.07 for B2, and 0.08 for B1. In this figure, error bars are also plotted to compare the standard deviation calculated for the four coefficients. These results do not show a dependence on geometrical modifications: all Cd_{std} values vary between 1.5% and 2% of the Cd_{mean}-benchmark value, while the Cl_{std} values fluctuate by about 0.1 units. The side force is not shown but there are no significant disturbances there due to the main flow being aligned with the x-direction.

The patterns observed for Cl_{mean} and Cd_{mean} are, to an extent, expected given the results shown in the previous sections, where we observed that grooved geometries did not cause large disturbances on a local or large scale. This, added to the fact that the benchmark is fully symmetric, leads to the near-zero effects in Cl_{mean}. On the other hand, the larger pressure effects on the top surface exerted by the bump geometries, Figure 8, differ enough from the benchmark to cause the largest variations.

Regarding Cd_{mean} disturbances, we stated that when examining Figures 7–10, there are no clear pressure disturbances on the front and rear sides of the cylinder, meaning that changes in drag may originate from local effects on the wrinkled surface. This assumption is supported by the logical observation that extra added obstacles (bumps) increase the characteristic length D and consequently drag, such as the ancillary modifications commented on in Ref. [13]. This also agrees with a close inspection of the plots in Figure 8, in which Cp_{mean} takes relative positive values at the immediate front cells of each bump, whereas it takes near-zero values at their adjacent rear cells. These pressure differences

are similar for all the bump geometries, which would explain the low variation in Cd_{mean} between these modifications, from 4% to 8%, despite the higher pressure differences caused by B3 and B4 in the flat zones that affect the lift. In other words, the inclination of triangular shapes leads to a greater surface area being exposed in the mainstream direction, allowing for a higher drag force than the square and circular bumps.

These deductions seem contradictory to previous reports addressing grooved surfaces with a similar relative size, which reported notable drag and lift reductions at lower Re (see references [18,19] in Section 1). The difference is related to the fact that these modifications disturb the pressure at the rear side. This could happen because (i) a more aerodynamic main body allows a visible effect due to the equispaced wrinkles, even for small modifications (see, for example, Figure 5 in Ref. [18] (p. 525), and Figure 12 in Ref. [19] (p. 14)) or (ii) the wrinkle is located at a position at which it can provoke a large effect (see, for example, the contrast between the two locations of the same wrinkle in Figure 9 in Ref. [18] (p. 529)). In the following subsection, we further discuss the contrast observed when implementing grooves and bumps into the model, while exploring and reporting alternative configurations for special purposes.

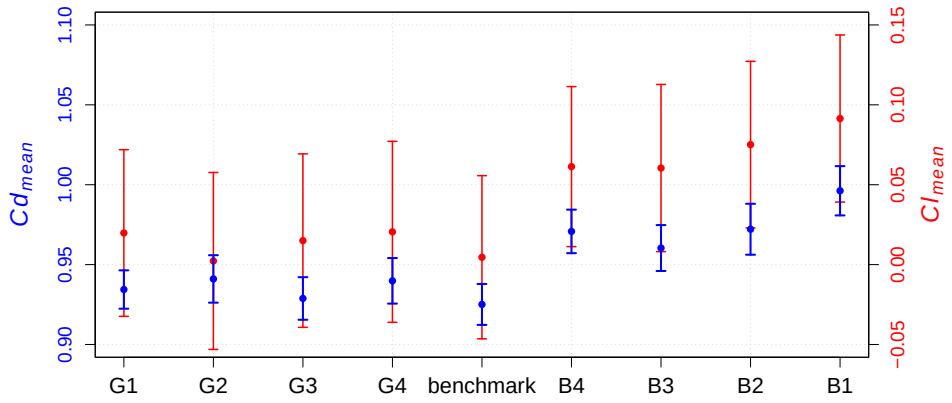


Figure 9. Comparison of the aerodynamic coefficients drag Cd (blue) and lift Cl (red) for all the geometries. Time-averaged values $(\cdot)_{mean}$ are plotted as filled circles, while their standard deviation values $(\cdot)_{std}$ are shown as error bars.

4.3. One-Dimensional Effects: Passive Control Along the Wrinkled Side

As described above, the wrinkles on the cylinder configure particular pressure and velocity fields. Therefore, it is of interest to understand how these two variables relate to vorticity. In an attempt to answer this question, this subsection examines the relationship between the pressure and velocity fields through U_{mean}, Cp_{mean}, U_{std}, Cp_{std}, and Ω_{mean}, in the immediate zones of the top cylinder surface shown in Figure 8. In addition, the relationship between these flow characteristics and the energy dissipation rate ϵ is explored.

Employing Bernoulli's equation and Formula (3) for incompressible flows, we derived the following relationship between Cp_{mean} and velocity,

$$Cp = 1 - U^2. \tag{6}$$

Then, when the local velocity U increases, Cp decreases.

Figure 10 depicts the joint behavior of Cp_{mean} and U_{mean} as a function (in color) of the auxiliary variable of distance ξ for each geometry considered in the simulation. This variable represents the minimum distance from the recording point of the mid-top surface to the nearest wrinkle. In this way, the points plotted in cyan are inner grooves or bumps, respectively; points in blue fall within the flat zones of the top surface; and those in black correspond to the front and rear sides. For either configuration, we can see that $U_{mean} = 0$ and $Cp_{mean} = 0.84$ on the left end (front) of the cylinder at $(X, Y) = (-2, 0)$; this is followed by a rapid increase in U_{mean} and a decrease in Cp_{mean} as functions of X for values of X around -2 until they settle down to what we call the "stabilization" zone. This decay in

the value of Cp_{mean} is also observed in Figure 8. After moving away from the stabilization in the right end of the cylinder and for coordinates in the neighbourhood $X = 2$, Cp_{mean} and U_{mean} exhibit values around -0.1 and 0.1, respectively, according to Figure 7, which was expected since the most dynamic flow–cylinder interactions occur at the left end, and hence we only see residual motion of the fluid at the right end.

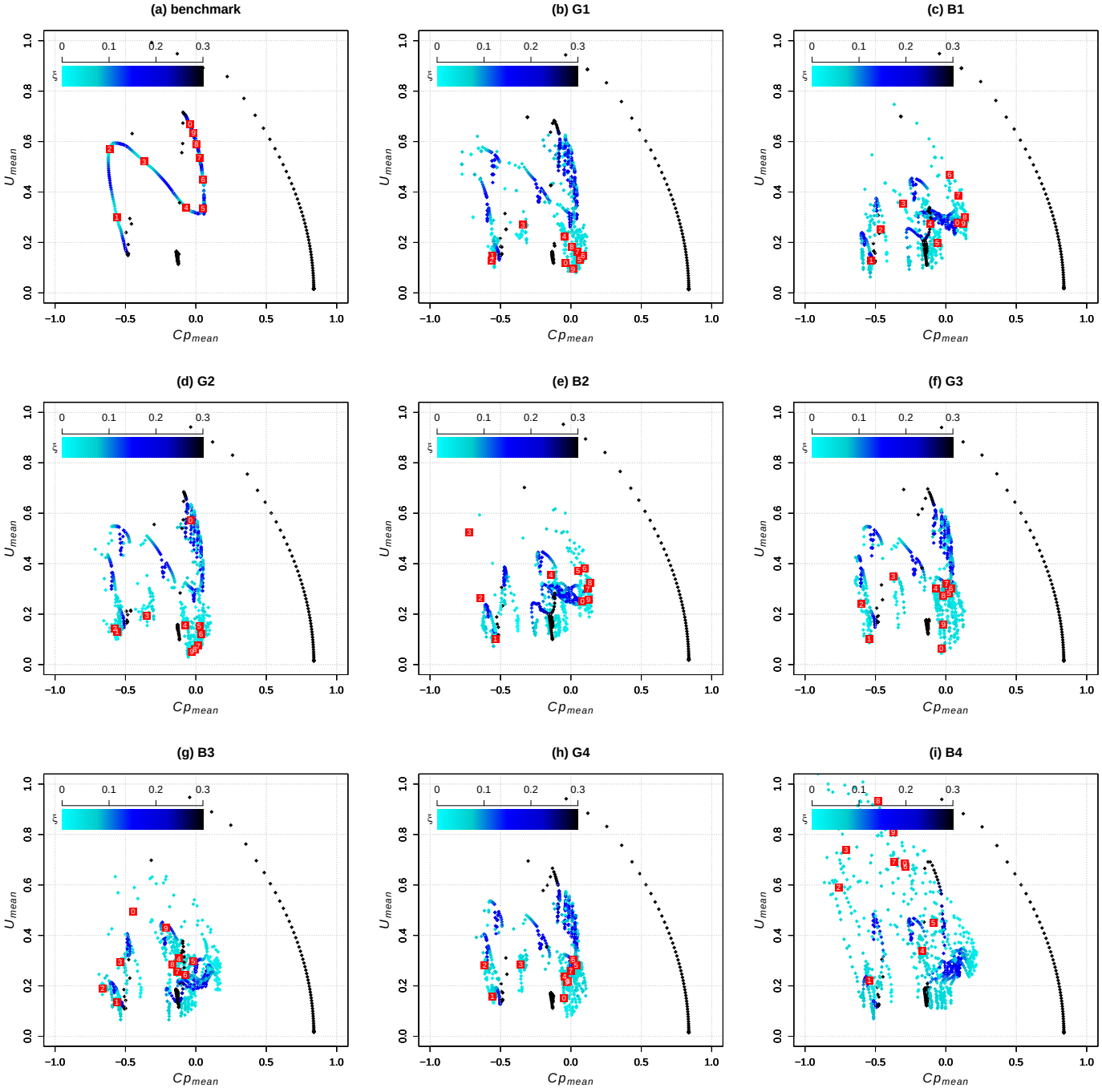


Figure 10. Time-averaged scatter plot of U vs. Cp along the top surface drawn in Figure 8. Benchmark (**a**). Grooves (**b**,**d**,**f**,**h**). Bumps (**c**,**e**,**g**,**i**). ξ values are shown by the color scale. Numerals i inside red squares indicate the point corresponding to the i-th wrinkle.

Figure 10a, corresponding to the benchmark, exhibits the most regular pattern between Cp_{mean} and U_{mean}; it resembles a sigmoid curve. In this case, Cp_{mean} decreases as U_{mean} increases and vice versa, except in between the inflection points around $X = -1.2$ (around the second wrinkle) and $X = 0$ (between the fourth and fifth wrinkle). The coordinates

X of these inflection points match the inflection points of Cp_{mean} observed in Figure 8a. These points define three distinguishable clusters in Figure 10a: the mean velocity U_{mean} increases before the first inflection point and after the second one, while it decreases at the intermediate X-coordinates. Therefore, U_{mean} inversely mirrors the behavior of Cp_{mean} for the benchmark. In Figure 10b,d,f,h, corresponding to grooved cylinders, the clusters limited by the inflection points can also be identified. In these cases, the mean velocity decays around the grooves, taking values around $U_{mean} \in (0.1, 0.2)$ for G1 and G2 (except in the 10th groove in G2) and around $U_{mean} \in (0.1, 0.3)$ for G3 and G4. The patterns observed replicate across the tested groove geometries, and the variability inside each cluster is roughly the same; thus, we conclude that the forms in each of these plots correspond to the sigmoid curve of the benchmark, disarranged by the grooves. This observation is supported by the results observed in Figure 8 for the Cp_{mean} domain. In the case of the latter, corresponding to Figure 10c,e,g,i, the sigmoid curve is altered to a higher degree. In this case, the clusters induced by the inflection points can also be identified, but they overlap. Despite this, the location of points in blue indicates that the velocity–pressure relationship is similar for all of these geometries in the flat and bumped zones, except for B4. It is worth noting that the mean velocity in the bumps is highly unsteady, with values of $U_{mean} \in (0.1, 0.5)$ for $B1$–$B3$ and $U_{mean} \in (0.2, 0.9)$ for $B4$. Notably, the case shown in Figure 10i, for the geometry $B4$, indicates that circular bumps induce the most chaotic behavior in the flow. Therefore, in spite of $B4$, the presence of wrinkles produces lower values of U_{mean} compared to the benchmark.

Figure 11 illustrates the relationship between Cp_{std} and U_{std} as a function of the distance ξ for each geometry considered in the simulation. Figure 11a shows the benchmark. In this plot, we can identify four data clusters around the coordinates X: (i) for X very near $X = 2$ and $X = -2$; (ii) X between -2 and -0.75; (iii) X between -0.75 and 0; (iv) X between 0 and 2. The first cluster forms at both ends of the cylinder and relates to the closest point to the origin (with the lowest variation: for the left end, Cp_{std} and U_{std} mostly take values near 0, while for the right end, $Cp_{std} \approx 0.025$ and $U_{std} \in (0.025, 0.075)$. Note that the data outside of the first cluster describe a curve. The second cluster is located at the low end of the curve and falls further away than the third wrinkle in relation to the point where the curve starts to rise at the U_{std} coordinate and backward at the Cp_{std} coordinate. The third cluster spans from the end of the second cluster to the point where the curve moving along the U_{std} coordinate starts descending after the position of the fifth wrinkle. The fourth cluster starts at the tail of the curve, and it moves downward and reaches the peak of the curve, where we see an abrupt decay in the velocity's standard deviation inside this cluster between the position of the fifth and sixth wrinkles; Figure 7 suggests that this is a transition zone between the highly dynamic first half of the cylinder and the less active second half, as pointed out in Section 4.1. Figure 11a also shows that the standard deviation of the pressure coefficient Cp_{std} is, on average, higher for the first part of the cylinder, which contrasts with the behavior of the second part of the object.

Figure 11b,d,f,h seem to display a distorted version of Figure 11a, although one could argue that the clusters recognized in Figure 11a are also present in these plots, but showing higher local variance in the clusters. Another consequence of the referred distortion is that measurements in the grooved cylinders follow the patterns observed in Figure 11a: the standard deviations Cp_{std} increase from 1 to 3 before starting to decrease. On the other hand, the standard deviation measured in the neighborhood of the grooves depict a line; for G1–G2, these measurements are below the mean line of the points, while for G3–G4, they are near the mean line. The difference in terms of U_{std} between the first and second half of the cylinder is higher than in the benchmark. Finally, in Figure 11c,e,g,i, it is not possible to identify any clear cluster associated with bump geometries. Most of the data points in these figures fluctuate around a backbone line, except for B4, in which case a line seems to fit well for the cases $Cp_{std} < 0.20$ but not for $Cp_{std} > 0.20$. Measurements in the bumps there are not described by a line. Similarly to the records taken for mean values, Figure 11i suggests that the geometry B4 induces the most turbulent behavior.

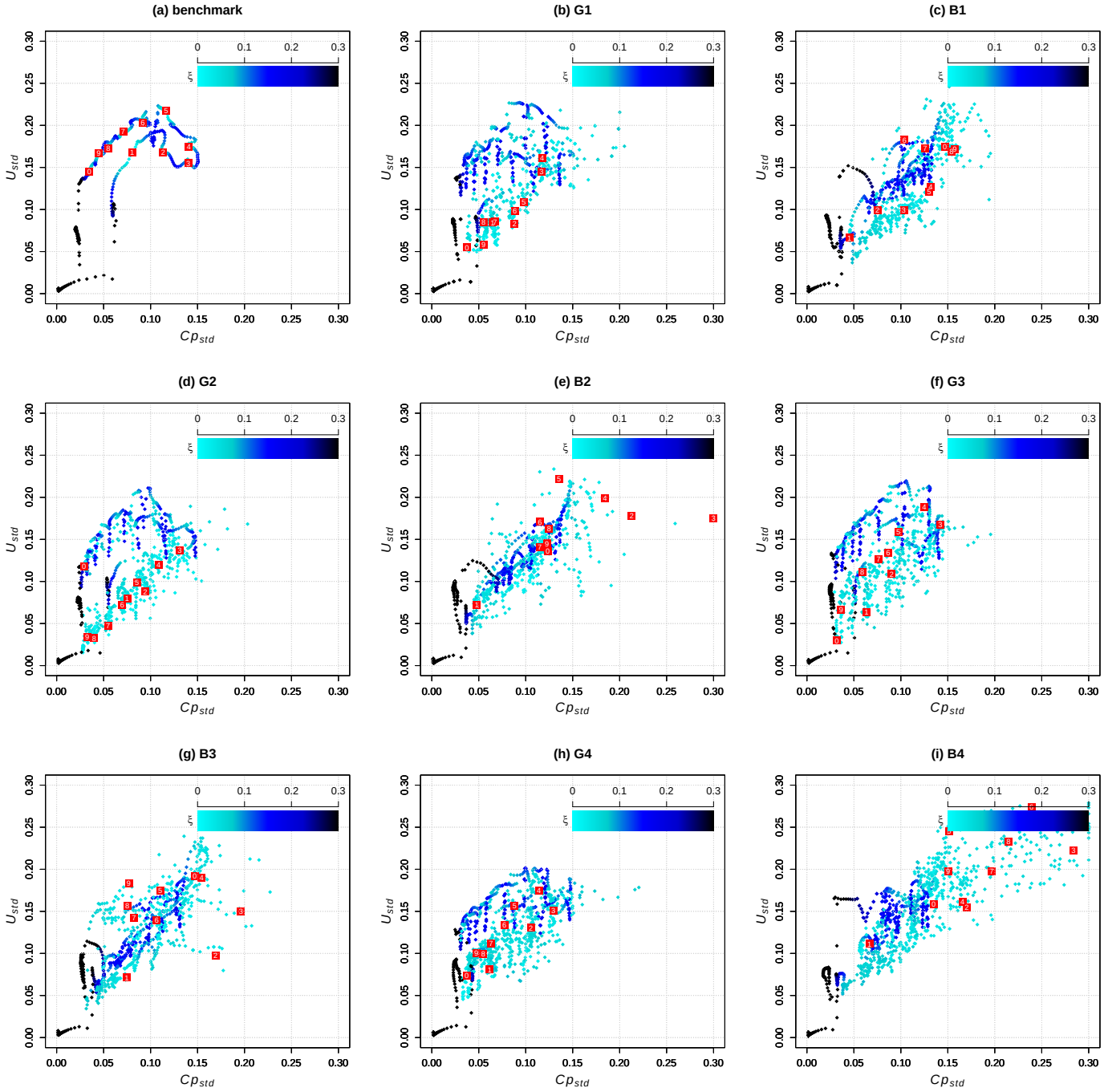


Figure 11. Time-averaged-variation scatter plot of U vs. Cp for the nine cases. Same notation as for Figure 10.

Moving on, there are different ways to compute the energy dissipation rate, depending on the restrictions on the flow. Since we used the Spalart–Allmaras model (1), this study employs the turbulent viscosity ν_t as a proxy for such a quantity, which is a non-physical variable that qualitatively characterizes the turbulent flow, by relating ϵ to $\Delta\mathbf{U}_{mean}$ according to

$$\epsilon \sim \nu_t \cdot (\Delta\mathbf{u}_{mean})^2, \tag{7}$$

see Landau and Lifshitz [40]. Another formula to consider is given by Ref. [41],

$$\tilde{\nu} = \sqrt{\frac{3}{2}} u_{mean} I l_t, \qquad \nu_t = \tilde{\nu} f_{\tilde{\nu}1}, \tag{8}$$

where l_t is the turbulent length scale (or the characteristic turbulent length), while I, $\tilde{\nu}$ and $f_{\tilde{\nu}1}$ are defined in Section 2.

In this context, Figure 12 presents the joint behavior of the mean energy dissipation, expressed by $N_{t_{mean}}$, the mean velocity U_{mean}, and the mean vorticity Ω_{mean}. The most striking result here is that, in all the cases, the data points $(U_{mean}, N_{t_{mean}})$ lie over rays converging to the origin, with a gradient bounded by the ray associated with the benchmark, which suggests that the wrinkles control the dissipation of energy on the top surface. In relation to this, Equation (8) implies that variations in the turbulence intensity I, length scale l, and function $f_{\tilde{\nu}1}$ determine the various gradients shown in Figure A1. Moreover, for the benchmark, most of the measurements follow a line, with the exception of data points that, once tracked, are related to the front $X = -2$ and rear sides $X = 2$, plus some other points around the inflection observed at $X = 0$, where the reattachment of the flow is discussed in Sections 3 and 4.1. This linear relationship establishes a direct link between the mean velocity and the energy dissipation rate. Furthermore, we also observe that vorticity (color scale) increases proportionally to the value of the velocity.

Regarding prototypes with grooves, Figure 12b,d,f,h show a more established relationship between $N_{t_{mean}}$ and U_{mean}. Additionally, the measurements at the position of the grooves reveal an energy dissipation $Nt_{mean} < 2 \times 10^{-6}$, except for G3 and one value in G2. Likewise, for geometries with bumps, Figure 12c,e,g,i show that the measurements of (U_{mean}, Nt_{mean}) also define less dense and better defined rays. This added to the fact that all modified geometries reduce dissipation, and hence vorticity is also affected by the presence of wrinkles, showing higher values at the right ends of the lower rays. This performance is replicated in practically all case studies, at similar rates, only changing with the graphic coordinates, which suggests that vorticity is strongly related to flow velocity and energy dissipation. Such behavior yields a well-organized and stable flow, as seen in Figure 7. Notably, the case of B4 exhibits higher mean velocities (and vorticity) than in the other cases; besides, the data points define two rays, with all the measurements in the bumps being located on the lower ray.

To synthesize the observed performance, we rewrite Equation (8), and complement it with dimensional analysis, so that

$$\nu_t = c_1 l_t u_{mean}, \quad \text{with } c_1 = I f_{\tilde{\nu}1} \sqrt{\frac{3}{2}}, \tag{9}$$

which expresses the linear relationship between turbulent viscosity and mean velocity shown in Figure 12, where the gradient of the rays is defined by $c_1 l_t$. It is worth noting that, since we are plotting the nearest cells to the objects, $f_{\tilde{\nu}1}$ does not change the value of the gradient, whereas Equation (9) suggests that the surface roughness induces small turbulent length scales l_t. This also holds for more defined rays determined across grooved geometries and for more disorganized clusters for the bumped cases.

Moreover, Figure 12 shows that the greater the gradient of the ray, the greater the vorticity, which can be inferred from Equation (9), since

$$\omega \sim \frac{u}{l_t} \tag{10}$$

and consequently,

$$\nu_t \sim c_1 {l_t}^2 \omega_{mean}. \tag{11}$$

In spite of the identified proportionality between ν_t and ω present in Equation (11), the cases in Figure 12 do not show such performance, as we observe an apparent inverse proportionality instead. The reason for this seems to be related to the high intensity of

vortex generation at low turbulence levels, i.e., ω is more dependent on ${l_t}^2$ than on ν_t, which indicates the presence of eddies instead of large vortexes.

In summary, Equations (10) and (11), inferred from our results, suggest that vorticity could be approximated with a function that depends on turbulent viscosity and flow velocity, while being independent from the wrinkled geometry. Figure 13a, which results from super-positioning the time-averaged values of all the geometries presented in Figure 12, supports the established relationship. Figure 13b shows that such a behavior is replicated for the time-averaged-variation values. The reader is referred to Figure A1 in Appendix A for additional evidence involving all cases.

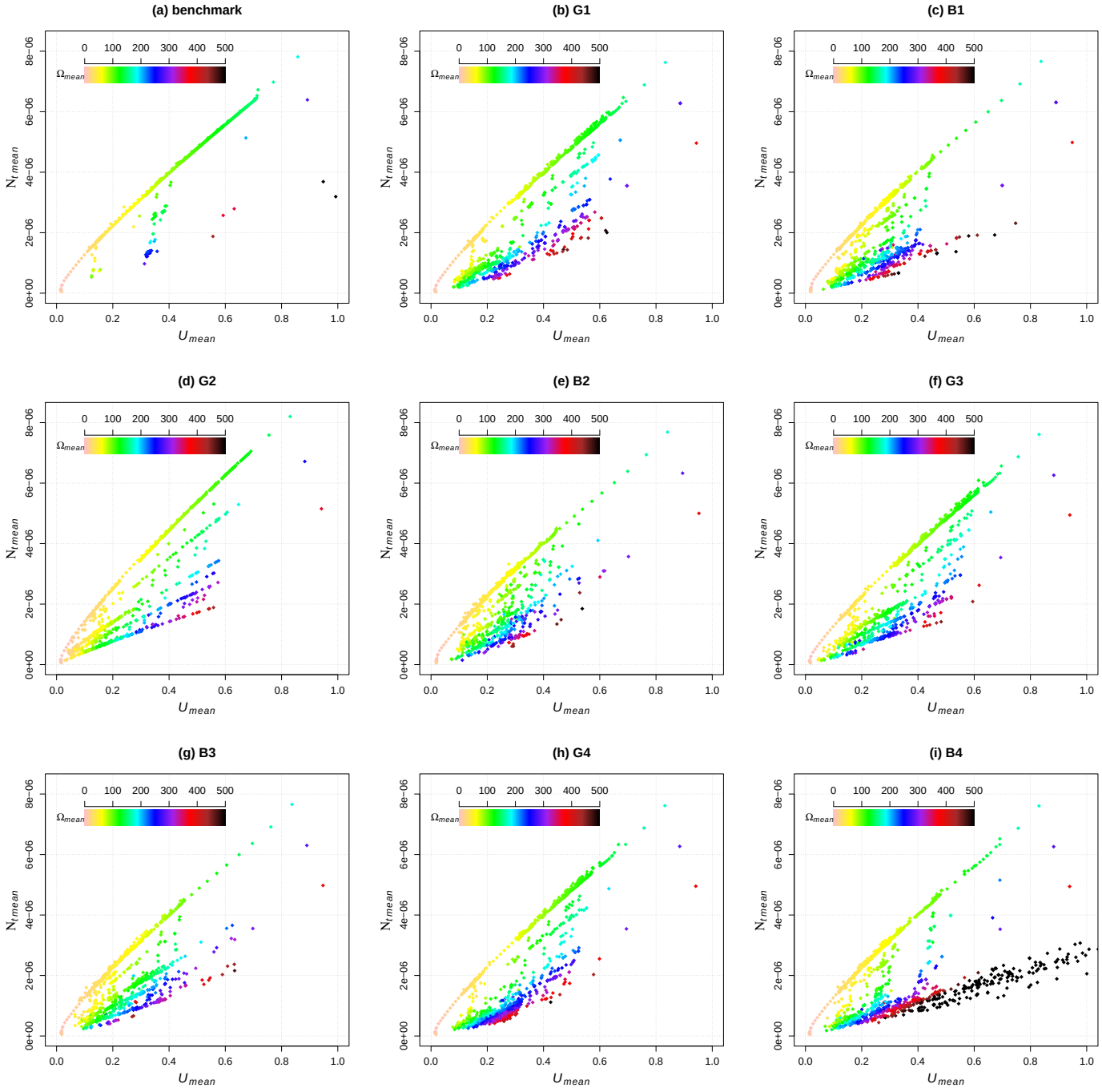


Figure 12. Time-averaged scatter plots of N_t vs. U for nine cases. Benchmark (**a**). Grooves (**b**,**d**,**f**,**h**). Bumps (**c**,**e**,**g**,**i**). Time-averaged values of Ω are indicated by the color scale. Points corresponding to wrinkles are not highlighted due to no significant behavior being found.

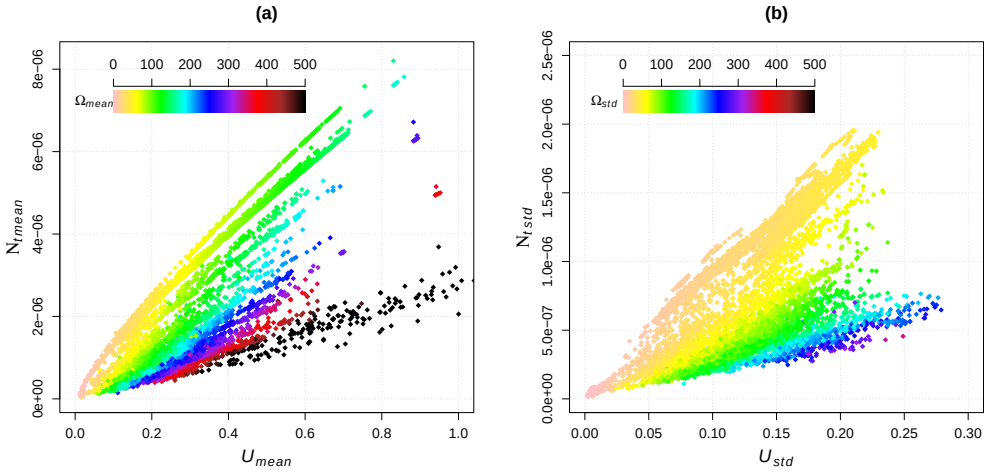


Figure 13. Superposition of scatter plots of the nine N_t vs. U cases. (**a**) Time-averaged and (**b**) time-averaged-variation. Same notation as for Figure 12.

4.4. Potential Applications and Future Work

The results obtained exemplify the effects that modified geometries could have on the aerodynamic performance of bluff bodies and their further engineering applications, as discussed in Section 1. The pressure patterns taking place on the top side of the cylinder could promote the use of composite structures in ocean engineering that could help to identify the optimum location of soft and tough materials. Further technological improvements could be informed by the patterns observed in the standard deviation of pressure fluctuation and including the vorticity and dissipation of energy charts shown in Figures 12 and 13. Furthermore, bump geometries could be manufactured on strong structures to define the degree of energy that these could absorb, while groove geometries could be useful for minimizing material cost since although they modify the aerodynamic performance, they do keep the force fields close to that of the benchmark. See Figure 8 for an example of the above observations. It is noticeable that grooves induce lower pressure disturbances than bumps over the region of reattachment; see, for example, Figure 8h,i (G4 vs. B4), where the former registers a peak Cp_{std} of around 10%, while the latter reaches 30% while crossing the zero line sporadically. These pressure fluctuations could induce excessive vibrations on flexible surfaces and membrane-like and cladding panels, none of where were modelled in this study.

Additionally, B1–B4 bump configurations could be considered for the prototyping of bus ancillaries, such as air conditioners, ceiling fans, or escape windows. The extra spaces on the bus would require less than 8% in drag. It should also be noted that our models are coarse approximations of the actual shape of a bus and that the effects produced by the floor wall are not considered. In turn, G1–G4 would be the choice in architectural design when the intention is not to significantly vary lift or drag.

Although the study of the wake is outside the scope of the present work, further research could follow on the positioning of objects in the far wake, given the asymmetric inflow that they would perceive. Future research could also involve big data analysis to characterize the time fluctuations of the flow, for which the addition of non-equispaced wrinkles could help to identify additional controlling parameters and their effect on the data recorded.

5. Conclusions

This paper presents a systematic study of flow around a rectangular cylinder at Re = 6×10^6, considering eight types of surface roughness on its top-surface. The wrinkled surfaces include prismatic grooves/bumps equispaced in the main flow direction.

Our concluding remarks about this study are summarized as follows:

- All of the proposed rough surface configurations cause local flow disturbances such as separation and reattachment, which at the micro-scale produce a sawtooth pressure pattern of pressure along the wrinkled surface. Therefore, variations in the aerodynamic coefficients with respect to the benchmark derive from mechanisms that determine the accumulation of pressure around the grooves/bumps. The largest increments in the drag are reached through the implementation of triangular bumps in model B1, which amounts to 8% with respect to the benchmark. In turn, the mean lift increases by 0.08 units, whereas no significant changes to the standard deviation were observed for either the drag or lift forces.
- This investigation puts forward an alternative visualization technique to scrutinize time-averaged and time-averaged-variation spaces of pressure–velocity, and turbulent viscosity–velocity corresponding to the wrinkled surface. For the pressure–velocity spaces, we observed two different clusters when plotting data points recorded on geometries with grooves and bumps. For the viscosity–velocity spaces, the curves fit a straight line for the benchmark, but split into multiple rays when introducing any type of roughness, with the grooved geometries G1–G4 being the least affected.
- The differences in flow patterns and aerodynamic coefficients determined in this study could help in tackling problems induced by the flow–structure interaction. We speculate that similar methodologies could benefit other engineering applications such as mechanical, maritime, and beyond.

Author Contributions: Conceptualization, M.A.A.-L. and F.H.-Z.; Data curation, M.A.A.-L. and F.H.-Z.; Formal analysis, M.A.A.-L., F.H.-Z., P.M.-V. and J.U.M.-U.; Funding acquisition, M.A.A.-L. and F.H.-Z.; Investigation, M.A.A.-L., F.H.-Z. and J.U.M.-U.; Methodology, M.A.A.-L., F.H.-Z. and P.M.-V.; Project administration, F.H.-Z.; Resources, M.A.A.-L.; Software, M.A.A.-L.; Supervision, F.H.-Z. and P.M.-V.; Validation, F.H.-Z., P.M.-V. and J.U.M.-U.; Visualization, M.A.A.-L. and F.H.-Z.; Writing—original draft, M.A.A.-L. and J.U.M.-U.; Writing—review & editing, F.H.-Z. and P.M.-V. All authors have read and agreed to the published version of the manuscript.

Funding: This research was funded by Consejo Nacional de Humanidades, Ciencias y Tecnologías (CONAHCyT) grant number 839412.

Data Availability Statement: The raw data supporting the conclusions of this article will be made available by the authors on request. The data are not publicly available due to their large size.

Acknowledgments: The authors thankfully acknowledge the computer resources, technical expertise and support provided by the Laboratorio Nacional de Supercómputo del Sureste de México, CONAHCyT member of the Network of National Laboratories. The second and fourth authors thank FCFM-UNACH and CIMAT, respectively, and CONAHCyT for the support through the program "Investigadoras e investigadores por México", Cátedras 873 and 783. The third author gratefully acknowledges the support of The Royal Society towards the mobility grant IES\R1\221087.

Conflicts of Interest: The authors declare no conflict of interest.

Abbreviations

The following abbreviations are used in this manuscript:

CFD	Computational Fluid Dynamics
DDES	Delayed Detached Eddy Simulations
FreeCAD	Free, Open-source 3D Computer-Aided Design
FVM	Finite Volume Method
GAMG	Geometric-algebraic multi-grid solver
LES	Large Eddy Simulations

OpenFOAM	Open Field Operation and Manipulation software
PISO	Pressure Implicit with Splitting of Operators solver
PPCR	Preconditioned pipelined conjugate residuals
RAS	Reynolds-Average Simulations
SA	Spalart–Allmaras turbulence model
STL	Stereolithography file format
VIVACE	Vortex Induced Vibration for Aquatic Clean Energy

Appendix A

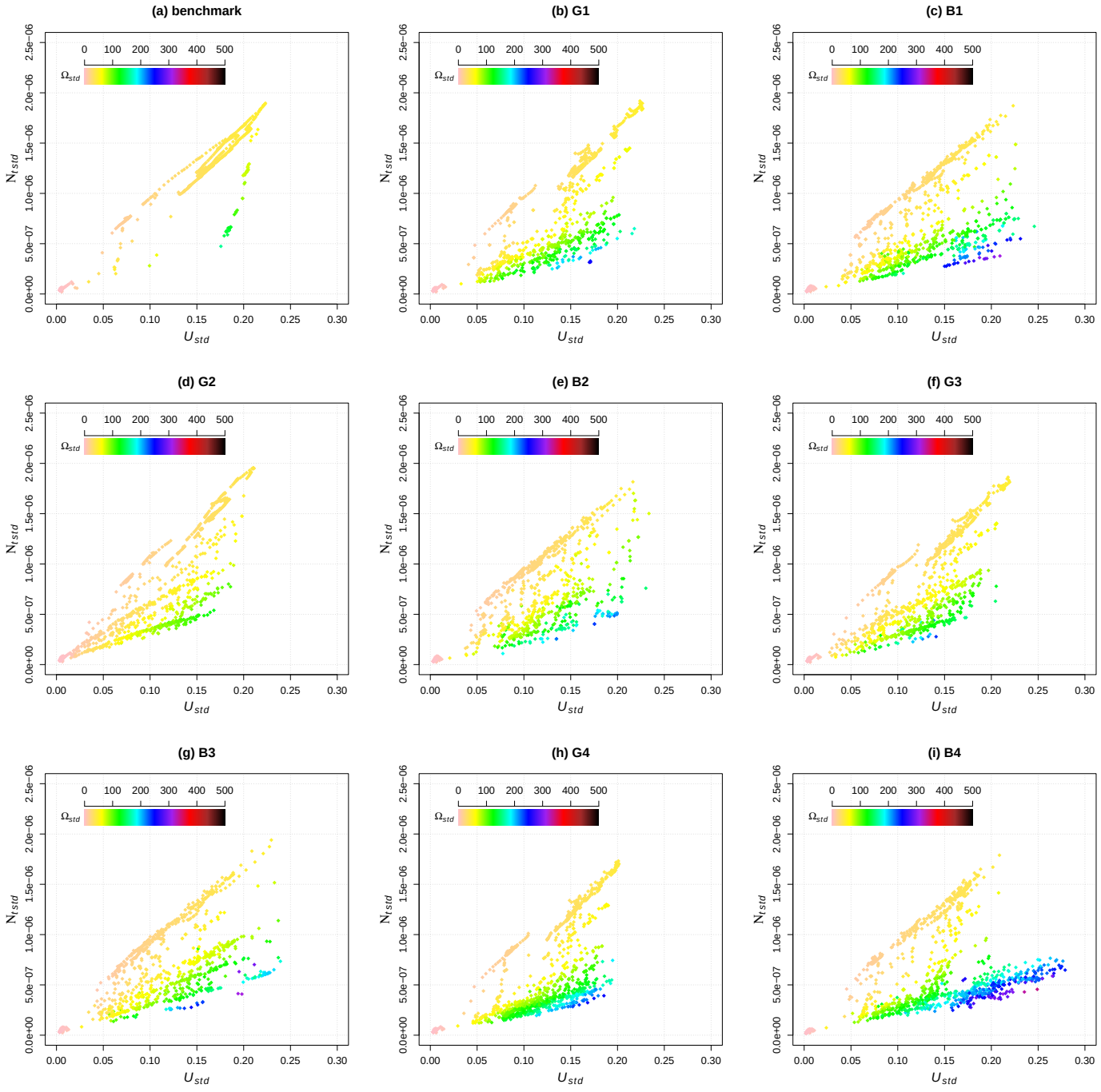


Figure A1. Time-averaged-variation scatter plot of N_t vs. U for the nine cases. Same notations than for Figure 10.

References

1. Ding, L.; Bernitsas, M.M.; Kim, E.S. 2-D URANS vs. experiments of flow induced motions of two circular cylinders in tandem with passive turbulence control for 30,000 < Re < 105,000. *Ocean Eng.* **2013**, *72*, 429–440. [CrossRef]
2. Lv, Y.; Sun, L.; Bernitsas, M.M.; Jiang, M.; Sun, H. Modelling of a Flow-Induced Oscillation, Two-Cylinder, Hydrokinetic Energy Converter Based on Experimental Data. *Energies* **2021**, *14*, 827. [CrossRef]
3. Bernitsas, M.M.; Raghavan, K.; Ben-Simon, Y.; Garcia, E.M.H. VIVACE (Vortex Induced Vibration Aquatic Clean Energy): A New Concept in Generation of Clean and Renewable Energy From Fluid Flow. *J. Offshore Mech. Arct. Eng.* **2008**, *130*, 041101. [CrossRef]
4. Raghavan, K.; Bernitsas, M. Experimental investigation of Reynolds number effect on vortex induced vibration of rigid circular cylinder on elastic supports. *Ocean Eng.* **2011**, *38*, 719–731. [CrossRef]
5. Lee, J.; Xiros, N.; Bernitsas, M. Virtual damper–spring system for VIV experiments and hydrokinetic energy conversion. *Ocean Eng.* **2011**, *38*, 732–747. [CrossRef]
6. Lee, J.; Bernitsas, M. High-damping, high-Reynolds VIV tests for energy harnessing using the VIVACE converter. *Ocean Eng.* **2011**, *38*, 1697–1712. [CrossRef]
7. Shi, X.; Dong, J.; Yan, G.; Zhu, C. Flow around a Rectangular Cylinder Placed in a Channel with a High Blockage Ratio under a Subcritical Reynolds Number. *Water* **2021**, *13*, 3388. [CrossRef]
8. Modi, V.; Hill, S.; Yokomizo, T. Drag reduction of trucks through boundary-layer control. *J. Wind. Eng. Ind. Aerodyn.* **1995**, *54–55*, 583–594. [CrossRef]
9. Chowdhury, H.; Moria, H.; Ali, A.; Khan, I.; Alam, F.; Watkins, S. A Study on Aerodynamic Drag of a Semi-trailer Truck. *Procedia Eng.* **2013**, *56*, 201–205. [CrossRef]
10. Damissie, H.Y.; Babu, N.R. Aerodynamic Drag Reduction on Locally Built Bus Body using Computational Fluid Dynamics (CFD): A Case Study at Bishoftu Automotive Industry. *Int. J. Eng. Res. Technol.* **2017**, *6*, 276–283.
11. Anantha Raman, L.; Rahul Hari, H. Methods for Reducing Aerodynamic Drag in Vehicles and thus Acquiring Fuel Economy. *J. Adv. Eng. Res.* **2016**, *3*, 26–32.
12. Altaf, A.; Omar, A.A.; Asrar, W. Passive drag reduction of square back road vehicles. *J. Wind Eng. Ind. Aerodyn.* **2014**, *134*, 30–43. [CrossRef]
13. Chilbule, C.; Upadhyay, A.; Mukkamala, Y. Analyzing the Profile Modification of Truck-trailer to Prune the Aerodynamic Drag and its Repercussion on Fuel Consumption. *Procedia Eng.* **2014**, *97*, 1208–1219. [CrossRef]
14. Mohamed-Kassim, Z.; Filippone, A. Fuel savings on a heavy vehicle via aerodynamic drag reduction. *Transp. Res. Part D Transp. Environ.* **2010**, *15*, 275–284. [CrossRef]
15. Jin, Y.; Cheng, Z.; Han, X.; Mao, J.; Jin, F. VLES of drag reduction for high Reynolds number flow past a square cylinder based on OpenFOAM. *Ocean Eng.* **2019**, *190*, 106450. [CrossRef]
16. Mazellier, N.; Feuvrier, A.; Kourta, A. Biomimetic bluff body drag reduction by self-adaptive porous flaps. *C. R. Mécanique* **2012**, *340*, 81–94. [CrossRef]
17. Malekzadeh, S.; Mirzaee, I.; Pourmahmoud, N.; Shirvani, H. The passive control of three-dimensional flow over a square cylinder by a vertical plate at a moderate Reynolds number. *Fluid Dyn. Res.* **2017**, *49*, 025515. [CrossRef]
18. Mariotti, A.; Buresti, G.; Gaggini, G.; Salvetti, M.V. Separation control and drag reduction for boat-tailed axisymmetric bodies through contoured transverse grooves. *J. Fluid Mech.* **2017**, *832*, 514–549. [CrossRef]
19. Qi, J.; Qi, Y.; Chen, Q.; Yan, F. A Study of Drag Reduction on Cylinders with Different V-Groove Depths on the Surface. *Water* **2022**, *14*, 36. [CrossRef]
20. Marshall, J. Drag measurements in roughness arrays of varying density and distribution. *Agric. Meteorol.* **1971**, *8*, 269–292. [CrossRef]
21. Chappell, A.; Van Pelt, S.; Zobeck, T.; Dong, Z. Estimating aerodynamic resistance of rough surfaces using angular reflectance. *Remote Sens. Environ.* **2010**, *114*, 1462–1470. [CrossRef]
22. Chakroun, W.; Al-Mesri, I.; Al-Fahad, S. Effect of Surface Roughness on the Aerodynamic Characteristics of a Symmetrical Airfoil. *Wind Eng.* **2004**, *28*, 547–564. [CrossRef]
23. Wang, M.; Yang, C.; Li, Z.; Zhao, S.; Zhang, Y.; Lu, X. Effects of surface roughness on the aerodynamic performance of a high subsonic compressor airfoil at low Reynolds number. *Chin. J. Aeronaut.* **2021**, *34*, 71–81. [CrossRef]
24. Aguirre-López, M.A.; Hueyotl-Zahuantitla, F.; Martínez-Vázquez, P. Passive Control Measures of Wind Flow around Tall Buildings. *Buildings* **2024**, *14*, 1514. [CrossRef]
25. Aguirre-López, M.A.; Hueyotl-Zahuantitla, F.; Martínez-Vázquez, P. Advances in Numerical Data Visualization of Flow around a Square Cylinder. *Symmetry* **2024**, *16*, 32. [CrossRef]
26. Jadhav, C.R.; Chorage, R.P. Modification in commercial bus model to overcome aerodynamic drag effect by using CFD analysis. *Results Eng.* **2020**, *6*, 100091. [CrossRef]
27. OpenFOAM. OpenCFD Release OpenFOAM v2012. 2020. Available online: https://www.openfoam.com/news/main-news/openfoam-v20-12 (accessed on 1 May 2022).
28. FreeCAD. Version 2018. Available online: https://www.freecadweb.org/ (accessed on 1 October 2022).
29. Young, D.F.; Munson, B.R.; Okiishi, T.H.; Huebsch, W.W. Elementary Fluid Dynamics—The Bernoulli Equation. In *A brief Introduction to Fluid Mechanics*, 5th ed.; Welter, J., Ed.; John Wiley & Sons, Inc.: Hoboken, NJ, USA, 2011; Chapter 3, pp. 68–101.

30. OpenFOAM v2012. Spalart-Allmaras Delayed Detached Eddy Simulation (DDES). 2020. Available online: https://www.openfoam.com/documentation/guides/v2012/doc/guide-turbulence-des-spalart-allmaras-ddes.html (accessed on 1 May 2022).
31. OpenFOAM v2012. Spalart-Allmaras Detached Eddy Simulation (DES). 2020. Available online: https://www.openfoam.com/documentation/guides/v2012/doc/guide-turbulence-des-spalart-allmaras-des.html (accessed on 1 May 2022).
32. OpenFOAM v2112. pisoFOAM Solver. 2018. Available online: https://www.openfoam.com/documentation/guides/latest/doc/guide-applications-solvers-incompressible-pisoFoam.html (accessed on 10 December 2023).
33. Issa, R. Solution of the implicitly discretised fluid flow equations by operator-splitting. *J. Comput. Phys.* **1986**, *62*, 40–65. [CrossRef]
34. Issa, R.; Gosman, A.; Watkins, A. The computation of compressible and incompressible recirculating flows by a non-iterative implicit scheme. *J. Comput. Phys.* **1986**, *62*, 66–82. [CrossRef]
35. Spalart, P.; Allmaras, S. A one-equation turbulence model for aerodynamic flows. In *30th Aerospace Sciences Meeting and Exhibit*; American Institute of Aeronautics and Astronautics: Reno, NV, USA, 1992; pp. 1–22. [CrossRef]
36. NASA Langely Research Center. Turbulence Modeling Resource. The Spalart-Allmaras Turbulence Model. 2020. Available online: https://turbmodels.larc.nasa.gov/spalart.html (accessed on 1 March 2022).
37. CFD Online. Turbulence Intensity. 2022. Available online: https://www.cfd-online.com/Wiki/Turbulence_intensity (accessed on 1 March 2022).
38. Spalart, P.R.; Deck, S.; Shur, M.L.; Squires, K.D.; Strelets, M.K.; Travin, A. A New Version of Detached-eddy Simulation, Resistant to Ambiguous Grid Densities. *Theor. Comput. Fluid Dyn.* **2006**, *20*, 181–195. [CrossRef]
39. OpenFOAM. Repository of Tutorials. 2016. Available online: https://develop.openfoam.com/Development/openfoam/-/tree/master/tutorials (accessed on 1 May 2022).
40. Landau, L.D.; Lifshitz, E.M. *Fluid Mechanics: Volume 6 (Course of Theoretical Physics)*, 2nd ed.; Elsevier: Amsterdam, The Netherlands, 1987.
41. CFD Online. Turbulence Free-Stream Boundary Conditions. 2014. Available online: https://www.cfd-online.com/Wiki/Turbulence_free-stream_boundary_conditions#:~:text=Modified%20turbulent%20viscosity,-The%20modified%20turbulent&text=is%20the%20turbulent%20length%20scale.&text=in%20the%20freestream.,contain%20shear%20become%20fully%20turbulent (accessed on 1 August 2023).

Disclaimer/Publisher's Note: The statements, opinions and data contained in all publications are solely those of the individual author(s) and contributor(s) and not of MDPI and/or the editor(s). MDPI and/or the editor(s) disclaim responsibility for any injury to people or property resulting from any ideas, methods, instructions or products referred to in the content.